Impact of gyro-motion and sheath acceleration on the flux distribution on rough surfaces

K. Schmid*, M. Mayer, C. Adelhelm, M. Balden, S. Lindig, ASDEX Upgrade team

Max-Planck-Institut für Plasmaphysik, EURATOM Association, Boltzmannstraße 2, 85748 Garching b. München, Germany

PACS numbers: 52.40.Hf, 52.40.Kh, 52.65.Cc, 61.80.Jh

Abstract.

As was already observed experimentally, the erosion of tungsten (W) coated graphite (C) tiles in ASDEX-Upgrade exhibit regular erosion patterns on the μm rough surfaces who's origin is not fully understood: Surfaces inclined towards the magnetic field direction show strong net W erosion while surfaces facing away from the magnetic field are shadowed from erosion and may even exhibit net W deposition. This paper presents a model which explains the observed erosion/deposition pattern. It is based on the calculation of ion trajectories dropping through the plasma sheath region to the rough surface with combined magnetic and electrical fields. The surface topography used in the calculations is taken from AFM measurement of real ASDEX-Upgrade tiles. The calculated erosion patterns are directly compared to SEM images of the erosion zones from the same location. The erosion on surfaces inclined towards the magnetic field is due to ions from the bulk plasma which enter the sheath gyrating along the magnetic field lines, while the deposition of W on surfaces facing away from the magnetic field is due to promptly re-deposited W that is ionized still within the magnetic pre-sheath.

* Corresponding author (Klaus.Schmid@ipp.mpg.de)

1. Introduction

Global erosion, re-deposition and transport of first-wall materials have been studied extensively in ASDEX-Upgrade (AUG). W coated C tiles from the outer divertor of AUG were analyzed post-mortem after the 2007 campaign by ion beam analysis methods and secondary electron microscopy (SEM) in [1]. The SEM images revealed a very inhomogeneous W erosion pattern where areas on the μm rough surface that were inclined towards the magnetic field (='leading' surfaces) were fully eroded down to the C substrate. In contrast the parts of the rough surface facing away from the magnetic field (='shadowed' surfaces) showed less erosion and also signs of W deposition in these areas were found. A very similar result was already observed in the AUG divertor after the 2004-2005 campaign [2], and the same effect was observed with W marker stripes in the outer divertor of JET [3]. The presence of these inhomogeneous erosion patterns puts constraints on the minimal W coating thickness required to avoid exposure of the C substrate during an experimental campaign in a fusion experiment. Therefore an understanding of the underlying processes leading to these patterns is desirable. As was already discussed in [1] these patterns cannot be explained by the pure gyro motion of the impinging ions, since the gyro radius is much larger than the surface roughness which should lead to a homogenous flux- and therefore also erosion distribution.
In this paper a model will be presented that explains the erosion patterns by calculating the flux distribution of the impinging ions on the rough surface by tracing the path of the ions from the gyro motion in the bulk plasma through the E×B drift in the sheath region until the impact on the surface. The rough surface topography data used in the calculations are taken from an atomic force microscope (AFM) scan of a small sample cut from a W coated C tile taken from the outer divertor of AUG. The calculated erosion patterns are compared to SEM images taken at the exactly same location as the AFM image.
These model calculations will show that the strong electric fields in the plasma boundary sheath affect the trajectories of the ions close to the surface, leading to oblique impact angles which in turn result in an inhomogeneous flux and erosion distribution. It will further show that promptly re-deposited W that is ionized within the magnetic pre-sheath after being sputtered from the surface has a very different impact angle spectrum compared to ions arriving from the bulk plasma. Promptly re-deposited W impinges almost along the surface normal, resulting in an essentially homogeneous flux distribution. This flux distribution together with the low impact energies and resulting low sputter yields explains the deposition of W on the shadowed surface areas.
The paper will first present the matching of the SEM erosion images with the AFM topography data. Then the applied model of the plasma sheath region and the calculation of the particle traces will be presented. Finally the flux and erosion distributions on the rough surface will be discussed.

2. Experimental erosion patterns on W coated C

A sample was taken from a W coated C marker tile from the outer strike point area of AUG (Bgr. 1, s-coordinate 1099.8 mm, see [1] for a cross-sectional view of the AUG divertor and the s-coordinate system) and had an initial W coating thickness of about 1500 nm. The marker tile was exposed for the whole 2007 campaign, which had 2620 s plasma in divertor configuration. This marker tile was used to determine the net mean W erosion, which was about 220 nm at the sample position. The 2007 campaign was the first campaign with a full-W AUG, and the concentration of C in the plasma was $< 1\%$. There were no boronizations during this campaign, and the boron concentration in the plasma was usually below the detection limit.

An SEM image of the W erosion pattern is shown in Fig 1. The SEM image was recorded with secondary electrons (SE). These exhibit a contrast with the nuclear charge of the surface elements due to the different secondary electron yields: C rich areas appear dark and W rich areas appear bright. The black arrow in Fig 1 indicates the approximate direction of the magnetic file which points essentially along the x-axis. The erosion pattern visible in Fig 1 is very inhomogeneous: On the leading surface areas the W layer is complete eroded exposing the underlying C substrate, while on the shadowed surface areas the W layer is still intact. Such an inhomogeneous erosion pattern was already previously observed at the outer divertor of AUG [2], and was also observed in the outer JET divertor [3]. There is a slight tilt angle $\alpha \neq 90°$ between the rows of leading surfaces and the magnetic field direction which already hints towards the influence of E×B forces on the particle trajectories responsible for eroding the W at these leading surfaces.

To establish a direct link between the erosion pattern and the topography of the rough surface, a mark (the letter "F" in Fig. 1) was cut into the surface using a focused ion beam (FIB). The size of this mark (about 5×8 μm^2) was chosen in such a way, that the mark is still visible in an optical microscope. In addition, about 35 μm long pointers (outside of the viewing area of Fig. 1) were cut into the surface for easier locating the mark. Then the sample was transferred to an atomic force microscope (AFM). AFM measurements were performed in AC mode with a MFP-3D system from Asylum Research. AC 160TS cantilevers from Olympus were used. In the AFM the same location marked by the "F" was found. Four individual AFM scans with scan areas of 90×90 μm^2 at a scan rate of 0.1 Hz and some overlap between the individual scan areas were performed. These individual scans were superimposed to a final AFM topography scan of 140×150 μm^2. The sample surface was inclined by about 3° due to a mechanical miscut. This was corrected by subtracting a plane from the raw AFM data.

newline The 3D topography information is overlaid by the 2D SEM image of the erosion pattern in Fig. 2. The green arrow again shows the approximate magnetic field direction. The areas marked in red correspond to the areas of full W erosion in Fig. 1, nicely showing that the erosion is confined to the leading surfaces. The surface roughness of the sample is of the order of a few μm, as can be seen in Fig. 2. The roughness appears overemphasized in Fig. 2 due to the different scaling in the z- vs. the x- and y- directions.

The AFM data in Fig. 2 depicts the final eroded rough surface which is different from the original pristine surface prior to exposure in AUG. However to peak erosion on these surfaces is $\approx 1\mu$m and the average erosion is even lower. Therefore for a feature height of $\approx 5 - 10\mu$m one can still assume that this surface is a good representation of the original rough surface and can thus be used as an input parameter in the calculations described in this paper.

3. Modeling particle trajectories in the sheath

In order to model the 3D trajectories of the impinging ions on the rough surface the magnetic and electric fields in the plasma boundary close to the surface have to be approximated. The coordinate system used in the calculations is shown in Fig. 3. The rough surface is located in the X-Y plane with its average surface normal pointing upwards along the Z-axis. The magnetic field lies in the X-Z plane at an angle δ with respect to the x-axis. The electric field due to the sheath potential drop points along the -Z axis.
The aim of the paper was to describe to observed patterns in an as simple (Occam's razor) model as possible.Of course one could implement a much more sophisticated sheath model but as will become apparent in section 6 this is not necessary to explain the experimental findings. Therefore model assumes a collision free sheath with homogeneous electric field and operates in the trace impurity approximation i.e the impurity concentration is assumed to be low enough as not to change the local plasma parameters.

3.1. Modeling the electric fields in the plasma sheath

To simplify the equations of motion for the ions the plasma boundary was subdivided into three regions as shown in Fig. 4. The top region is the bulk plasma where only a magnetic field is present, inclined at an angle δ with respect to the rough surface. The second region is the magnetic pre-sheath (MPS) followed by the third region, the Debye sheath (DS) just above the rough surface. The electric field inside these two regions is assumed to be constant and determined by the respective potential drop divided by the width of the region. In region one the particles spiral on gyro orbits along the magnetic field lines. In the sheath (region two and three) the particle additionally undergos an ExB drift motion which adds a translational motion component along the ExB direction. The approximations applied to model the electric potential and field in the sheath are shown on the right hand side in Fig. 4. The total electrostatic potential drop in the sheath ΔU_S over MPS and DS is approximately constant (i.e does not depend on δ) and given by eq. 1 [4]. The individual potential drops in the MPS and DS depend on the magnetic field angle δ. For smaller δ's the potential drop in the DS decreases and a larger fraction of ΔU_S occurs in the MPS.

$$\begin{aligned} \Delta U_S &= \frac{1}{2}\frac{T_e}{e_0}\log\left(\frac{2\pi m_e\,(T_e+T_i)}{T_e m_i}\right) \qquad (1)\\ T_i, T_e &= \text{Ion and electron temperature respectively (eV)} \end{aligned}$$

m_i, m_e = Ion and electron mass respectively
e_0 = Elementary charge

The electric field E_{MPS} in the MPS is calculated based on the potential drop ΔU_{MPS} in the MPS and the width l_{MPS} of the MPS as shown in eq. 2 [4].

$$\begin{aligned}
\Delta U_{MPS} &= \frac{T_e}{e_0} \ln\left(\cos(\pi - \delta)\right) \\
l_{MPS} &= \sqrt{6}\left(\frac{c_s}{\omega}\right)\sin(\delta) \\
E_{MPS} &= \frac{\Delta U_{MPS}}{l_{MPS}}
\end{aligned} \tag{2}$$

$$\begin{aligned}
c_s &= \text{Plasma sound speed} = \sqrt{\frac{T_e + T_i}{2m_i}} \\
\omega &= \text{Gyro frequency} = \frac{e_0 q B}{m_i} \\
T_e &= \text{Electron temperature} \\
T_i &= \text{Ion temperature} \\
q &= \text{Ion charge state} \\
B &= \text{Toroidal magnetic field}
\end{aligned} \tag{3}$$

The potential drop ΔU_{DS} in the DS is calculated based on ΔU_S and ΔU_{MPS}, while the electric field E_{DS} in the DS is determined by the ratio of ΔU_{DS} and the width $l_{DS} = \lambda_{Debye}$ of the DS as in eq. 4 [4].

$$\begin{aligned}
\Delta U_{DS} &= \Delta U_S - \Delta U_{MPS} \\
l_{DS} &= \sqrt{\frac{\epsilon_0 T_e}{e_0 n_e}} \\
E_{DS} &= \frac{\Delta U_{DS}}{l_{DS}}
\end{aligned} \tag{4}$$

ϵ_0 = Vacuum permittivity
n_e = Electron density

The above formulas for the potential drops in the MPS and DS are only valid for values of $\delta > 3°$. For more oblique angles the electric field becomes more complex and can no longer be assumed to be constant (see for instance [5]). While in fusion experiments values for $\delta << 3°$ are not uncommon, the calculations presented here will use a value of $\delta = 5°$ for simplicity. For a Deuterium (D) plasma with $T_e = T_i = 20$ eV, $n_e = 10^{18}\, m^{-3}$ and $\delta = 5°$ the electric fields are $E_{MPS} \approx 2 \times 10^4$ V/m and $E_{DS} \approx 2 \times 10^5$ V/m. The width of the MPS is ≈ 2000 μm, while the width of the DS is $\lambda_D \approx 30$ μm. In the frame of this model it is assumed that the dimension of the Debye sheath, i.e. the Debye length λ_D, is larger than the average surface roughness (≈ 5 μm in Fig. 2): In this case the surface roughness does not influence the electrostatic field. For cases where the amplitude of the roughness and λ_D are of the same order, the electrical field has to be calculated by a particle-in-cell code. This is for example the case for carbon-fiber composite (CFC) surfaces, which have a much larger mean roughness up to a few ten

μm and are used as plasma-facing material in the JET divertor [3]. These cases are beyond the scope of the model presented here.

3.2. Solving the equations of motion

To model the particle trajectories through the MPS or DS the motion of a particle in a E×B field as depicted in Fig. 3 has to calculated. The equations of motion (See for instance [6]) are given in eq. 5 for a particle moving in a E×B field with B = $(B_X, 0, B_Z)$ and E = $(0, 0, -E_Z)$ oriented as shown in Fig. 3.

$$\begin{aligned} \ddot{x}(t) &= \beta B_Z \dot{y}(t) \\ \ddot{y}(t) &= \beta \left(B_X \dot{z}(t) - B_Z \dot{x}(t) \right) \\ \ddot{z}(t) &= \beta \left(-B_X \dot{y}(t) - E_Z \right) \\ \beta &= \frac{q}{m} \text{ Charge to mass ratio} \\ E_Z &= \text{Z-Component of the electrical field } \vec{E} = (0, 0, E_Z) \end{aligned} \tag{5}$$

Eq. 5 has an analytical solution (determined by Mathematica$^{\text{TM}}$) which is given in the Appendix of this paper. For motion in the bulk plasma with only a magnetic field B = $(B_X, 0, B_Z)$ the equations of motion are identical except for the $-E_Z$ term which does then not occur in the equation for $\ddot{z}(t)$ In this $E_Z = 0$ case the particles simply spiral on gyro orbits.

3.3. Calculating particle traces

Based on the analytical solution of eq. 5, the trajectories of ions can be calculated given the appropriate initial values for velocity $\vec{v}_{init}$ and position $\vec{r}_{init}$. With respect to the initial values two cases were considered. Case 1: Particles entering the sheath region (i.e the MPS) on gyro orbits from the bulk plasma (= long range transport particles). Case 2: Sputtered particles originating from the rough surface which are ionized either within the MPS or within a distance from the rough surface smaller than their gyro radius (= promptly re-deposited particles).
For Case 2 the initial values have to be determined from their initial ejection from the surface according to a cosine distribution and their point of ionization. The direction $\vec{d}_{Cos}$ of $\vec{v}_{init}$ for case 2 is given directly by a sample from the cosine distribution from eq. 6.

$$\begin{aligned} \vec{d}_{Cos} &= (0, 0, 1) \cdot \mathbf{R}(\vartheta, (1, 0, 0)) \cdot \mathbf{R}(\varphi, (0, 0, 1)) \\ \vartheta &= \arcsin\left(\sqrt{r_\vartheta}\right) \\ \varphi &= 2\pi r_\varphi \\ \mathbf{R}(\alpha, \vec{r}) &= \text{Rotation matrix around axis } \vec{r} \text{ by angle } \alpha \\ r_\varphi, r_\vartheta &= \text{Uniform random numbers from 0-1} \end{aligned} \tag{6}$$

The magnitude of $\vec{v}_{init}$ is given by eq. 7

$$|\vec{v}_{init}| = \sqrt{\frac{2 \langle E_{Sput} \rangle}{m}} \tag{7}$$

$$\begin{aligned} \langle E_{Sput} \rangle &= \text{Mean energy of sputtered particles} \\ m &= \text{Mass of sputtered particle} \end{aligned}$$

For physical sputtering $\langle E_{Sput} \rangle$ is approximately half the surface binding energy, so $\approx$ 4.3 eV for W. The position of ionization $\equiv \vec{r}_{init}$ is assumed to be equally distributed between a distance of l_{DS} and l_{DS} + max(l_{MSP}, r_{Gyro}) where r_{Gyro} is the gyro radius of the sputtered W at charge state +1. No ionization below l_{DS}, i.e. inside the DS, is assumed due to the lack of electrons there and assuming that electron impact as the dominant ionization process. In reality the place of ionization will vary with distance from the surface, but the variations along max(l_{MSP}, r_{Gyro}) $\approx$ 1 mm will probably be small and are neglected for sake of simplicity in this model.

For Case 1, the long range transport particles, the initial values have to be determined from their gyro orbit motion as they enter the MPS. $\vec{r}_{init}$ is any position on the entrance of the MPS, but the direction of $\vec{v}_{init}$ depends on the phase angle Ω of the gyro motion as the particle enters the MPS [7]. Fig. 5 depicts the last gyro orbit as seen from the side and along the magnetic field, respectively. Ω is determined by the smallest distance Δ between the particle and the MPS prior to hitting the MPS boundary. For a large enough distance $\Delta = \Delta_{Max}$ the particle can perform one entire gyro orbit $\Omega = 2\pi$ prior to hitting the MPS (Case with $\Omega = \Omega_2$ in Fig. 5 b.)). For smaller values of $\Delta, (0 \leq \Delta \leq \Delta_{Max})$ Ω will be $< 2\pi$ (Case with $\Omega = \Omega_1$ in Fig. 5 b.)). For a given value of Ω, $\vec{v}_{init}$ for Case 1 can be calculated according to eq. 8

$$\begin{aligned} \vec{v}_{init} &= (v_{||}, V_{\perp}, 0) \cdot \mathbf{M} \qquad (8) \\ \mathbf{M} &= \mathbf{R}(\Omega, (1,0,0)) \cdot \mathbf{R}(\delta, (0,1,0)) \\ v_{||} &= \text{Velocity along magnetic field} \\ v_{\perp} &= \text{Velocity perpendicular to magnetic field} \end{aligned}$$

The values for $v_{||}$ and $v_{\perp}$ have to be chosen separately (see below).

To determine Ω one has to calculate the time difference t_{imp} between the impact on the MPS and the time when the particle has the distance Δ to the MPS at the start of its last gyro orbit. In the bulk plasma outside the MPS the equations of motion in the coordinate system aligned with the magnetic field, marked with an dash (x', y', z') in Fig. 5 a.) have the simple solution given in eq. 9

$$\begin{aligned} x'(t) &= v_{||} t \qquad (9) \\ y'(t) &= r_g \sin(\omega t) \\ z'(t) &= r_g \cos(\omega t) \\ r_g &= \text{Gyro radius} = \frac{m v_{\perp}}{q e_0 B} \end{aligned}$$

Once t_{imp} is known $\Omega = t_{imp}\omega$ can be calculated and inserted into eq. 8 to determine $\vec{v}_{init}$ for a given choice of $v_{||}$ and $v_{\perp}$. From the geometric consideration in Fig. 5 a.) follows equation 10, which relates Δ and t_{imp}.

$$\begin{aligned} \Delta &= \gamma + \varepsilon * \tan(\delta) - \frac{\varepsilon}{\cos(\delta)} \qquad (10) \\ \gamma &= v_{||} \left(\frac{\pi}{\omega} + t_{imp} \right) \\ \varepsilon &= r_g + r_g \cos(\omega \, t_{imp}) \end{aligned}$$

Due to the term $\cos(\omega\, t_{imp})$ eq. 10 has to be solved numerically for t_{imp}. The approximations made in [7] to determine t_{imp} were not applied here since the author could not follow the arguments leading to them. The numerical solution of eq. 10 always gives two solutions for Ω: The first solution is $\Omega \equiv 2\pi \equiv \Omega_{Max}$ which corresponds to the case $\Omega = \Omega_2$ in Fig. 5 b.). The second solution is $\Omega < 2\pi \equiv \Omega_{Min}$ which corresponds to the case $\Omega = \Omega_1$ in Fig. 5 a.). These two results for Ω limit the range of impact directions for the long range particles. Typical values for Ω_{Min} for C^{+4} or D^+ are $\approx 340°$, which means that light ions (with $\beta \approx 0.5$) almost finish one full gyro orbit before entering the sheath due to their high gyro frequency. This high value of Ω_{Min} also means that the directions of incidence for C^{+4} or D^+ span only a very narrow range, leading to rather sharp impact angle distributions (see section 4). For heavier ions (with $\beta << 0.01$) Ω_{Min} is $\approx 280°$ due to their lower gyro frequency. This wider range of possible incident directions means that long range transport heavy ions usually have a broader angular distribution (see also Fig. 6).

For the Case 1 initial values one has to choose values for $v_{||}$ and $v_{\perp}$, the velocities in the coordinate system aligned to the magnetic field of the gyrating particles in the bulk plasma prior to entering the sheath region. For D^+, the plasma majority ion, the logical choice is to set $v_{\perp}$ equal to the thermal velocity and $v_{||}$ equal to the sound speed c_s as in [7]. The thermal velocity is taken from a Maxwell distribution of velocities determined by the local electron temperature T_e and the mass of the ion m_i. For impurity ions like C, which are responsible for the observed W erosion, the same choice for $v_{\perp}$ can be made, setting it to its thermal velocity. The choice for $v_{||}$ is more difficult since it depends on whether or not the friction force has accelerated the impurity ion to the background plasma flow speed $\approx c_s$. Therefore the D plasma sound speed is an upper limit, but lower values are also possible. The influence of input parameter variations on particle traces, including variation of $v_{||}$, will be investigated in section 4.

Based on the above conditions for $\vec{v}_{init}$ and $\vec{r}_{init}$ the particle trajectories were calculated as follows: For the long range transport particles the trajectory starts at the entrance to the MPS with an initial velocity direction randomly chosen from $\Omega_{Min} \leq \Omega \leq \Omega_{Max}$. $v_{\perp}$ was randomly chosen from a Maxwellian velocity distribution given the ion mass and plasma temperature $T_e\,(\approx T_i)$. First the drop through the MPS to the entrance of the DS is calculated yielding an impact position and velocity at the DS entrance. Based on this impact data the drop through the DS onto the rough surface is subsequently calculated. The surface impact calculation returns the first intersection of the particle trajectory with the rough surface. For simple impact angle calculations also flat surfaces were considered applying the same method.

For the prompt re-deposited particles the calculation starts at the surface where the initially neutral particle is emitted with an initial velocity direction randomly chosen from a cosine distribution. It is subsequently ionized at a z coordinate (distance from surface along normal) z_{iz} which is chosen randomly from $l_{DS} \leq z_{iz} \leq \max(l_{MSP}, r_{Gyro})$. Therefore the start position for the ion trajectory potentially lies in the bulk plasma for cases where $r_g > l_{MPS}$. For those cases first the impact on the MPS was calculated yielding the position and velocity at the entrance to the MPS. The rest of the calculation is identical to that for the long range transport particles and also ends at the surface

yielding the impact position and velocity at impact.
The ratio r_F of the lorenz force to the electrostatic force in the MPS and DS is quite different. Assuming $v_\perp$ equal to the thermal velocity and using the central parameters from Tab. 1, r_F in the MPS becomes $r_F \approx 2$ and $r_F \approx 0.2$ in the DS. Thus the motion in the MPS is still dominated by lorenz force i.e particles still spiral on gyro orbits of essentially identical radius as in the bulk plasma, where as in the DS the electrostatic force dominates i.e the particles drop towards the surface along a parabola like trajectory. The dominating nature of the lorenz force would even have allowed to ignore the MPS in the trajectory calculations but is still included for completeness.
For higher magnetic fields, as will be present in ITER (≈ 5 T), the situation changes only in the DS. The electric field in the MPS is tied to the magnetic field via the gyro frequency in eq. 2 thus r_F in the MPS is constant with the magnetic field. In contrast r_F in the DS increases linearly with B and therefore for 5 T $r_F \approx 1$ in the DS. This means that the two forces become comparable at high magnetic fields. Still due to the small spatial extensions of the DS the particle do not spiral on gyro orbits.

4. Impact angle distributions

One of the key parameters characterizing the impact of the ions on rough surfaces is the impact angle. Therefore, in order to investigate the influence of the numerous input parameters on the ion trajectories, the variation of the impact angle and its distribution were calculated for varying input parameters. For these calculations a perfectly flat surface with no roughness was assumed. For the long range transport particles, $\vec{r}_{init}$ was chosen as $(0, 0, l_{MSP} + l_{DS})$, i.e. just at the entrance of the MPS. For the prompt re-deposited particles $\vec{r}_{init}$ was at a distance from $(0, 0, 0)$, equally distributed between l_{DS} and $l_{DS} + \max(l_{MSP}, r_{Gyro})$. The initial velocities were selected as described in section 3.3. The input parameters were varied around a central set of parameters show in Tab. 1. This central set of parameters was also used in the ray tracing calculations described in section 5 to determine the laterally resolved flux and erosion distributions. The impact angle α was calculated from the velocity vector at the time of impact $\vec{v}_{imp}$ on the surface according to eq. 11

$$\begin{aligned} \alpha &= \arccos\left(\frac{-\vec{v}_{imp} \cdot \vec{n}_{imp}}{|\vec{v}_{imp}| * |\vec{n}_{imp}|}\right) \\ \vec{n}_{imp} &= \text{Local surface normal vector at the position of impact} \end{aligned} \tag{11}$$

For the impact angle calculations on a flat surface, presented in this section, $\vec{n}_{imp}$ is always equal to the z-axis $(0, 0, 1)$. The resulting angular distributions using the "Central Value" input parameters in Tab. 1 are shown in Fig. 6. For the long range transport case D^+, and C^{+4} are shown. They impact the surface at a rather oblique angle of incidence with $\langle\alpha\rangle \approx 60°$. In contrast the promptly re-deposited W^{+1} ions impinge essentially along the surface normal with $\langle\alpha\rangle \approx 10°$. Also shown in Fig. 6 for comparison is the angular distribution for long range W^+ with an initial parallel velocity equal $\langle E_{Sput}\rangle$. It impinges on the surface at an angle of $\approx 40°$ somewhere in between the light long range particles and the prompt re-deposited W.

For all cases the particles impinge onto the surface essentially along straight lines. The radius of curvature ρ can be calculated according to eq. 12

$$\begin{aligned} \rho &= \frac{|\partial_t \vec{r}(t)|^3}{\partial_t \vec{r}(t) \times \partial_{t,t} \vec{r}(t)} \\ \vec{r}(t) &= (x(t), y(t), z(t)) \text{ Solution to the equations of motion} \end{aligned} \tag{12}$$

For the "Central Value" input parameters in Tab. 1 the radius of curvature is of the order of 0.5 to 1 mm, which is orders of magnitude larger than the surface roughness features.

The average impact directions are shown in Fig. 3. Due to the strong electrostatic field the particles do not impinge along the magnetic field direction, but are deflected along the z-axis. Due to the E×B forces the particles impinge not exactly in the plane defined by the z-axis and the magnetic field direction, but slightly sideways along the y-axis. This is the reason for the slight tilt angle observed in the erosion patterns described in section 2. The strong difference between the impact angles of long range transport (D^+, and C^{+4}) and the prompt re-deposited particles (W^{+1})is that they enter the sheath under very different conditions: As described in section 3.3 eq. 8 and 10 the long range transport particles enter the sheath region in a narrow range of velocity directions and are only slightly bent away from the magnetic field direction mainly by the electrostatic field in the DS. This results in oblique angles of incidence still dominated by the field line angle δ. In contrast the prompt re-deposited particles after being ionized within a gyro radius from the surface, essentially undergo 1/2 gyro orbit prior to impacting the DS and finally on the surface. At the end of this 1/2 gyro orbit their velocities point along the surface normal resulting in the observed low impact angles.

To investigate the influence of the sheath acceleration on the impact angle distribution a separate set of calculations was performed with no electric but only a constant, homogeneous magnetic field. The results are displayed in Fig. 7. For light impurities the impact of the electrostatic acceleration in the sheath is not large, but for heavy ions with $q/m \ll 1$ the influence is large. In particular for the slow, heavy prompt re-deposited W the angular distribution changes from a broad distribution centered around 45° to a narrow distribution centered around 85° in the presence of sheath acceleration.

To investigate the influence of the input parameters in Tab. 1 on the particle trajectories, the variations of the average impact angle due to variations of the parameters was calculated. The range of the parameter variations is given in the table row labeled "Variation range". Each range was sampled by 5 values and for each combination of values 100 impact angles were averaged and compared to the average impact angle obtained for the parameter set from table row "Central value". This huge data set is difficult to visualize. In Fig. 8 the histogram of the ratio of the average impact angle $\langle\alpha\rangle$ for a given parameter set to the average impact angle $\langle\alpha_{Cen}\rangle$ for the "Central value" parameter set is displayed for long range transport D^+, C^{+4} and prompt re-deposited W^{+1} ions. The standard deviation of $\langle\alpha\rangle$ over the entire range of parameter combinations is rather low $\approx 10 - 20\%$. This means that the results of the calculations presented in this paper are relatively insensitive to the input parameters listed in Table 1. The conclusions drawn in this paper therefore have a general validity for erosion processes on

rough surfaces in current fusion experiments. In future fusion experiments the magnetic field will be even higher (≈ 5 T in ITER). As was already mentioned in section 3.3 the ration r_F of the lorenz to the electrostatic force become equal in the DS at such high fields. For long range transport particles this leads to even more oblique angles of impact α since the particle trajectories follow more along the magnetic field line direction which has very oblique angle with respect to the surface. For the prompt re-deposited particles (e.g W^+1) the impact direction is still essentially along the surface normal with only very minor increase of α. Thus it can be concluded that the here described mechanism for inhomogeneous erosion on rough surface is most likely also to occur in ITER.

5. Variation of flux across rough surfaces

When a flux of particles impinges on a rough surface, then the flux density distribution is always inhomogeneous due to the different projections of the influx onto the individually oriented areas of the rough surface. Before going into the details of the flux distribution of particles dropping through the sheath potential, it is worth while to perform a few basic considerations on the variation of flux density on rough surfaces.

5.1. Basic considerations on the variation of flux on rough surfaces

When a flux of particles $\frac{\#}{m^2 s}$ impinges on a rough surface at an angle α with respect to the average surface normal $\langle\vec{n}\rangle$, then the flux varies due to three processes depicted in Fig. 9:

- Projection
- Self shadowing
- Long range shadowing

"Projection" describes the variation when an incident flux of particles passing through area A in Fig. 9 is projected onto an area A' on the surface. The resulting variation f_{proj} in flux distribution is given in eq. 13.

$$\begin{aligned} f_{proj} &= -\vec{\Gamma}\cdot\vec{n} \\ \vec{\Gamma} &= \Gamma_0 * \vec{d} \\ \vec{d} &= \text{Normalized direction vector} \\ \vec{n} &= \text{Local normalized surface normal} \end{aligned} \tag{13}$$

"Self shadowing" describes the "local" blocking of the incident particle flux by a feature on the rough surface. Its modification of the flux distribution is characterized by f_{sself} which is given in eq. 14.

$$f_{sself} = \begin{cases} 1 & -\vec{\Gamma}\cdot\vec{n} \geq 0 \\ 0 & -\vec{\Gamma}\cdot\vec{n} \leq 0 \end{cases} \tag{14}$$

"Long range shadowing" can not be described by a simple formula and has to be handled by ray tracing of the particle trajectories and recording their individual impact positions (see below).

For an incident flux impinging along a fixed direction $\vec{d}$, the variation in the flux is determined by the variation of the normal vector across the rough surface, i.e. by the f_{proj} parameter. The topography data from an AFM scan are just a function from $\mathbb{R}^2 \rightarrow \mathbb{R}$ which assigns a height z to each spatial location (x,y) on the rough surface. The surface normal at each spatial location (x,y) can then be calculated by eq. 15.

$$\begin{aligned} \vec{r} &= (x, y, z(x, y)) \\ \vec{n} &= \frac{\partial \vec{r}}{\partial x} \times \frac{\partial \vec{r}}{\partial y} \end{aligned} \tag{15}$$

After normalizing the results for $\vec{n}$ from eq. 15, the distribution of the normal vector components from the AFM topography data (displayed in Fig. 2) can be determined. The resulting distribution of the local surface normal vector components is shown in Fig. 10. The x and y components of the normal vector show a broad distribution which is symmetrically distributed around zero, while the z component has a very narrow distribution around values of ≈ 1. This is a quite typical result for a rough surface, where the normal vector mostly points upwards in the z-direction with only minor variations. To investigate the variation in the local particle flux for a given incident flux direction $\vec{d} = (d_x, d_y, d_z)$ on a rough surface with a surface normal vector component distribution as in Fig. 10 the propagation of the variations in n_x, n_y and n_z in f_{proj} has to be calculated. For simplicity and in order to obtain analytical results the distributions in Fig. 10 are approximated as poisson distributions of widths σ_x, σ_y and σ_z. Then Gaussian error propagation applied to f_{proj} yields the variation $\sigma\left(f_{proj}\right)$

$$\sigma\left(f_{proj}\right) = \sqrt{d_x\sigma_x + d_y\sigma_y + d_z\sigma_z} \tag{16}$$

As a consequence of eq. 16 for oblique impact angles with $\alpha \approx 90°$, where $d_z \approx 0$, the variation in the flux distribution across the rough surface is dominated by σ_x and σ_y, whereas for normal angle of incidence with $\alpha \approx 0°$ with $d_x \approx d_y \approx 0$ the variation in the flux distribution is dominated by σ_z. From the normal vector component distribution in Fig. 10 one can see that $\sigma_x \approx \sigma_y \gg \sigma_z$. Therefore oblique angles of incidence lead to a broad distribution of fluxes due to the comparatively large values of σ_x and σ_y, whereas for normal angles of incidence the variation in the flux is much smaller due to the small σ_z. Applying this relation to the average impact angles of long range transport and prompt re-deposited particles shown in Fig. 6 follows that the long range particles with their oblique angles of incidence will have large variations in their flux distribution across the rough surface, whereas prompt re-deposited particles with their normal angles of incidence will have an essentially homogeneous flux distribution across the surface. It is this difference between long range transport particles and prompt re-deposited particles that explains the experimental observation of strong erosion on leading surface areas together with deposition in shadowed areas: The W is eroded on the leading surfaces by light long range transport impurities like C^{+4} and is prompt re-deposited homogenously across the surface leading to deposition in shadowed areas.

5.2. Flux and erosion distributions from ray tracing and flux projection calculations

The basic processes that vary the flux distribution across a rough surface which were detailed in section 5.1 can be extended in order to include the influence of varying angles

of incidence within the impinging ion flux. Also the previously neglected influence of "Long range shadowing" can be included in the considerations by detailed ray tracing of the particle trajectories.

To calculate the flux distributions across the rough surface via ray tracing $\approx 9 \times 10^5$ particle trajectories were calculated as described in section 3. For the long range transport particles $\vec{r}_{init}$ was chosen as $(x, y, l_{MSP} + l_{DS})$ i.e. just at the entrance of the MPS. For the prompt re-deposited particles $\vec{r}_{init}$ was simply chosen as (x, y, h), with a randomly chosen h from $l_{DS} \leq h \leq max(l_{MSP}, r_{Gyro})$. The initial lateral coordinates (x,y) were varied within $-2Size \leq$x or y$\leq 2Size$ where Size is width of the AFM scan area. Due to the fact that $l_{MSP} \gg Size$ the particles launched at $\vec{r}_{init}$ traveled a large lateral distance of up to several mm before impinging on the surface. In order to calculate the corresponding impact on the rough surface from the AFM scan, periodic boundary conditions were applied in lateral direction which allowed to extend the rough surface to infinity. The initial velocities were selected as described in section 3.3. The result from these calculation were impact positions $\vec{r}_{imp}$ and the velocities at impact $\vec{v}_{imp}$. To calculate the flux distribution from these impact positions their spatial location (x_{imp}, y_{imp}) was binned into 100 bins in x and y direction. To relate this histogram to a real fluence $\Phi\,(m^{-2})$ or flux $\Gamma\,(m^{-2}s^{-1})$ each of the impinging particle in the simulations was assumed to correspond to $\eta = \frac{\Phi A}{N}$ particles or $\eta = \frac{\Gamma A}{N}$ particles/s, where A was the total AFM scan area and N the number of particles traced in the simulation. Based on η the flux Γ_j^e or fluence Φ_j^e of ion species e impinging on the j-th bin is given by

$$\begin{aligned}
\Gamma_j^e \text{ or } \Phi_j^e &= \eta \frac{m_j}{a_j} \cos(\alpha_j) \qquad (17)\\
m_j &= \text{Number of impacts of element e counted into bin j}\\
a_j &= \text{Surface area of bin j}\\
\cos(\alpha_j) &= \vec{n}_j \cdot \vec{z}\\
&= \text{Projection of bin area onto corresponding rough surface area}\\
\vec{n}_j &= \text{Local surface normal at rough surface area corresponding to bin-j}\\
\vec{z} &= \text{z-Axis vector}
\end{aligned}$$

To calculate the gross erosion flux $\Gamma_j^{\text{Ero by e}}\,(m^{-2}s^{-1})$ or the eroded areal density of W $\Phi_j^{\text{Ero by e}}\,(m^{-2})$ by incident ion species e in each bin the erosion flux due to each individual particle has to be determined and weighted by the appropriate η as in eq. 18

$$\begin{aligned}
\Gamma_j^{\text{Ero by e}} \textit{ or } \Phi_j^{\text{Ero by e}} &= \eta \frac{\cos(\alpha_j)}{a_j} * \sum_{i=1}^{m_j} Y^e(E_i, \gamma_i) \qquad (18)\\
\gamma_i &= \arccos\left(\frac{-(\vec{v}_{imp})_i \cdot \vec{n}_i}{|(\vec{v}_{imp})_i| * |\vec{n}_i|}\right)\\
&= \text{Local impact angle of the i-th particle}\\
\vec{n}_i &= \text{Local surface normal vector at i-th particle}\\
&\quad \text{impact position}\\
Y^e(E_i, \gamma_i) &= \text{W Sputter yield by element e}\\
&\quad \text{as function of energy and angle}
\end{aligned}$$

E_i = Impact energy of the i-th particle calculated from $(\vec{v}_{imp})_i$

$(\vec{v}_{imp})_i$ = Velocity vector on impact of the i-th particle

To determine $Y^e(E_i, \gamma_i)$ for D, C and W ions on W the Monte Carlo code TRIDYN [8] was used to calculate the W sputter yields by D, C and W for a range of energies (20 to 1000 eV) and impact angles (0 to 89°). TRIDYN assumes a perfectly flat surface during its sputter yield calculations. The calculated 2D array of sputter yields was fitted by the product of the Bohdansky formula for the energy dependence and the Yamamura formula for the angular dependence of the sputter yield to obtain a formula for $Y^e(E_i, \gamma_i)$ [9, 10].

To calculate the effective W sputter yield on bin-j $Y_j^{\text{Eff by e}}$ by the incident flux of ion species e taking into account the energy and angle distribution in the incident flux the results for $\Phi_j^{\text{Ero by e}}$ from eq. 17 have to be divided by Φ_j^e from eq. 18:

$$Y_j^{\text{Eff by e}} = \frac{\Phi_j^{\text{Ero by e}}}{\Phi_j^e} \tag{19}$$

To compare the simulation results to the experimentally found erosion patterns, the total erosion depth has to be calculated. The erosion depth is given by the net removed W areal density divided by the bulk W density assuming erosion of pure W by the impinging species. Only W is being deposited, since according to [11] the impinging C will not deposit under the plasma conditions in Tab. 1. Taking erosion by D^+ and C^{+4}, self sputtering, and prompt re-deposition of W into account, the following relation holds for the net W erosion flux from the j-th bin $\Gamma_{net,j}^{ERO}$

$$\begin{aligned}\Gamma_{net,j}^{ERO} &= \left(\Gamma_j^{ERO,byD}(1-\nu_c)\right) + \left(\Gamma_j^{ERO,byC}(\nu_c)\right) \\ &\quad + \Gamma_{net,j}^{ERO} * R * Y_j^{\text{Eff by W}} - \left(\Gamma_{net,j}^{ERO} * R(1-\text{Refl})\right)\end{aligned} \tag{20}$$

$\Gamma_j^{ERO,byD}, \Gamma_j^{ERO,byC}$ = Erosion flux due to impact of D and C^{+4} respectively

ν_c = Fraction of C^{+4} in the incident flux

R = Fraction of eroded W that is prompt re-deposited

$Y_j^{\text{Eff by W}}$ = Effective W self sputtering yield due to prompt re-deposited W at bin j

Refl = W reflection yield

Solving equation 20 for $\Gamma_{net,j}^{ERO}$ and multiplying the result by the total exposure time of the W surface to the plasma, yields the net removed W areal density. Thereby the gross erosion fluxes $\Gamma_j^{ERO,byD}$ and $\Gamma_j^{ERO,byC}$ are calculated according to equation 18 and the effective self sputtering due to prompt re-deposited W, $Y_j^{\text{Eff by W}}$, is calculated from eq. 19. The fraction R of eroded W that is promptly re-deposited and the carbon fraction ν_c in the incident plasma flux are free parameters that are adjusted to fit the experimentally observed erosion patterns and the maximum erosion depth of 1.5 μm. ν_c and R are to some extent collinear parameters, since an increase in the total erosion due to an increase of ν_c can be partially compensated by increasing the re-deposition by increasing R. A reasonable fixed value of R = 0.3 was chosen and ν_c was varied to

reproduce the maximum erosion depth. Although more effort could be put to estimate a value for R, due to the collinearity of R and ν_c the experimental data can be reproduced for any value of R with a reasonable $\nu_c < 1\%$. Therefore the choice of R does not affect the conclusions of this paper. Due to the low energies of the promptly re-deposited W^{+1} ions the reflection yield is almost constant with angle and so a value of Refl ≈ 0.1 was used.

6. Flux distribution results

The erosion of W in fusion experiments is dominated by light impurity ions like C^{+4} [12, 11]. Fig. 11 shows the calculated distributions for C^{+4} ions (Ion flux: a.) Effective W sputter yield b.) and gross erosion flux c.)). Overlayed as black hatched areas on each of the graphs is the experimentally determined W erosion pattern which corresponds to the red shaded areas in Fig. 2. The flux and gross erosion flux values in Fig. 11 a.) and c.) are calculated for $\Gamma = 1$ $C^{+4}\, m^{-2} s^{-1}$ which makes it easy to identify the peaking factors. The flux peaking factor is $\approx 2-3$ comparing the mean flux to the maximum local flux. The gross erosion flux peaking is slightly lower with a factor of ≈ 2, because the erosion flux in eq. 18 is essentially given by the incident flux multiplied by the angular dependent sputtering yield, which has an $\approx \cos(\gamma_i)^{-1}$ dependence through the Yamamura formula. This means that the highest flux is obtained on surface areas with normal vectors pointing towards the incident flux $\cos(\gamma_i) \approx 1$, while the sputtering yield is increased on surfaces where the incident flux impinges at an oblique angle $\cos(\gamma_i) \ll 1$. However, for $\gamma_i \approx 2\pi$ both the flux and the sputtering yield go to 0. Therefore for a prediction of the erosion pattern a correct implementation of the angular dependence of the sputtering yield is necessary, the flux variation alone does not suffice.
The same calculation as for C^{+4} was performed for D^{+}. The results show a very similar flux distributions with similar peaking factors. However, due the low energy the effective sputtering yield and resulting gross W erosion are essentially zero.
Fig. 12 shows the flux distribution of promptly re-deposited W^{+1} overlayed with the experimentally determined erosion pattern (showed again as a black hatched area). As was already expected from the angular distribution shown in Fig. 6 and the considerations in section 5.1 the promptly redeposited W shows no flux peaking exceeding the statistical variations which can be expected from the statistics in each bin. Also no correlation to the experimental erosion pattern is found. Thus it can be concluded that promptly re-deposited material is indeed deposited uniformly over the rough surface. The effective self-sputtering yield and the gross erosion flux due to the prompt re-deposited W were also calculated and showed no significant spatial variations. Therefore no plots are displayed. The average effective self-sputtering yield is $\approx 10^{-4}$, which is low but not unexpected due to the low energies of the impinging W^{+1} ions. They are only accelerated by the sheath (MPS + DS) and thus end up with $\approx 3 * T_e = 60$ eV.
Given the calculated spatial distribution of the gross erosion fluxes $\Gamma_j^{ERO,byD}, \Gamma_j^{ERO,byC}$ and the effective self sputter yields $Y_j^{\text{Eff by W}}$, eq. 20 can be used to calculate the net

W erosion flux $\Gamma_{net,j}^{ERO}$, and from this the total erosion depth (see section 5.2) given the plasma exposure time $\tau_{Plasma} = 2620$ s. The averaged total plasma ion flux Γ during the whole campaign, required for the calculation of η in section 5.2, was determined from the total ion fluence measured by Langmuir probes and was $2.87 \times 10^{22} m^{-2} s^{-1}$. Using these input data and the result from eq. 20, the total W erosion depth was calculated. ν_c was varied so that the maximum erosion depth was 1.5 μm i.e. equal to the initial thickness of the W coating. This procedure yielded a value of $\nu_c \approx 0.3\%$. Due to total erosion of the initial W layer at the areas with maximum erosion this value for ν_c may be slightly too low. The resulting spatial distribution of the net erosion depth is shown in Fig. 13. There is an excellent match between the experimentally determined and calculated areas of high erosion. Deviations between calculation and experiment are probably due to matching problems of the AFM topography to the SEM erosion pattern image. Also it must be kept in mind that the experimental erosion pattern is a combination of variations in the erosion rate and in the initial thickness of the layer. Given these uncertainties, the match between the calculation and the experimental data confirms the model proposed in this paper to explain the experimentally observed spatial variations in the erosion rate.

7. Conclusions

The reason for inhomogeneous erosion patterns on rough surfaces exposed to a magnetized plasma with a magnetic field at an oblique angle to the surface was investigated. The W erosion pattern obtained from an SEM image of the surface after plasma exposure is matched to the topography information from an AFM scan. Erosion occurs predominantly at leading surface areas. In addition there is evidence that deposition occurs in shadowed areas. The question that arises is, how net erosion can occur at leading edges at the same time as net deposition occurs in shadowed areas. A model describing these inhomogeneous erosion patterns is proposed. The model is based on the fact that particles impinging on the surface have to travel through high electric fields in the plasma boundary sheath, leading to deflections of the particles resulting in an impact angle relative to the surface normal which is very different from that of the magnetic field. The model further distinguishes between long range transport particles from the bulk plasma and eroded particles which are promptly re-deposited. The former impinge on the surface at oblique angles of incidence, whereas the latter impinge essentially along the surface normal. It is shown from a fundamental treatment of the flux distributions on rough surfaces, that this difference in the impact angles leads to a very inhomogeneous flux distribution for the long range transport particles, whereas the promptly re-deposited particles have a homogeneous flux distribution. This impact angle based argument is further confirmed by detailed particle trajectory calculations. The erosion patterns obtained from this trajectory calculation are in very good agreement with the experimentally observed net erosion patterns.

It can be therefore concluded from the model, that the experimentally observed inhomogeneous erosion patterns with maximum erosion on leading surfaces are due to the long range transport particles, whereas the deposition in shadowed areas is due

to the promptly re-deposited particles.

8. Appendix

8.1. Solution to the equations of motion

The solution of the equation of motion from eq. 5 is

$$
\begin{aligned}
x(t) = & \frac{1}{2\beta\zeta^2}\left(2B_X^2B_Z\left(\beta B_Z\left(2r_x^0+tv_x^0\right)+v_y^0\right)+2\beta B_X^4\left(r_x^0+tv_x^0\right)+\right.\\
& 2B_Z\left(\beta B_Z^3r_x^0+\sqrt{\zeta}B_Zv_x^0\sin(\phi)+B_Z^2v_y^0-\zeta v_y^0\cos(\phi)\right)-\\
& B_XB_Z\left(E_Z\left(t^2\beta^2B_Z^2+2\cos(\phi)-2\right)+2v_z^0\left(\sqrt{\zeta}\sin(\phi)-t\beta B_Z^2\right)\right)+\\
& \left.t\beta B_X^3B_Z\left(2v_z^0-tE_Z\beta\right)\right)\\
y(t) = & \frac{1}{\beta\zeta^2}\left(\zeta\left(2B_Zv_x^0\sinh^2\left(\frac{\psi}{2}\right)+\beta\zeta r_y^0-\sqrt{\gamma}v_y^0\sinh(\psi)\right)-\right.\\
& \left.B_X\left(E_Z\left(t\beta\zeta+\sqrt{\gamma}\sinh(\psi)\right)+\zeta v_z^0(\cosh(\psi)-1)\right)\right)\\
z(t) = & \frac{1}{2\beta\zeta^2}\left(B_X^2\left(2\left(\beta B_Z^2\left(2r_z^0+tv_z^0\right)+\sqrt{\zeta}v_z^0\sin(\phi)\right)+\right.\right.\\
& E_Z\left(-t^2\beta^2B_Z^2+2\cos(\phi)-2\right)+\\
& \beta B_Z^4\left(2\left(r_z^0+tv_z^0\right)-t^2E_Z\beta\right)+2\beta B_X^4r_z^0+\\
& 2B_X\left(t\beta B_Z^3v_x^0-\sqrt{\zeta}B_Zv_x^0\sin(\phi)-B_Z^2v_y^0+\zeta v_y^0\cos(\phi)\right)+\\
& \left.\left.2B_X^3\left(t\beta B_Zv_x^0-v_y^0\right)\right)\right.\\
\beta \quad = & \, q/m\\
\zeta \quad = & \, B_X^2+B_Z^2\\
\phi \quad = & \, t\beta\sqrt{\zeta}\\
\gamma \quad = & \, -B_X^2-B_Z^2\\
\psi \quad = & \, t\beta\sqrt{\gamma}\\
\vec{r}_{init} = & \, (r_x^0,r_y^0,r_z^0)\\
\vec{v}_{init} = & \, (v_x^0,v_y^0,v_z^0)
\end{aligned}
\tag{21}
$$

[1] M Mayer, M Andrzejczuk, and R Dux et al. *Phys. Scr.*, T138:014039, 2009.
[2] M. Mayer, V. Rohde V, G. Ramos, E. Vainonen-Ahlgren, and J. Likonen et al. *Phys. Scr.*, T128:106, 2007.
[3] M. Mayer, J. Likonen, J. P. Coad, H Maier, M. Balden, and S. Lindig et al. *J. Nucl. Mater.*, 363–365:101, 2007.
[4] P. C. Stangeby. *The plasma boundary of magnetic fusion devices*. IOP Pulishing, Bristol BS1 6BE, 2000.
[5] I. I. Beilis and M. Keidar. *Physics of plasmas*, 5:1545, 1998.
[6] P. C. Stangeby. *University Physics with Modern Physics with Mastering Physics*. Addison Wesley, 11th edition edition, 2003.
[7] M. Shimada and T. Ohkawa. *J. Nucl. Mater.*, 266-269:906, 1999.
[8] W. Möller, W. Eckstein, and J. P. Biersack. *Computer Physics Communications*, 51 No. 8:355, 1988.
[9] J. Bohdansky. *Nucl. Instrum. and Meth. B*, 2:587, 1984.
[10] W. Eckstein and R. Preuss. *J. Nucl. Mater.*, 320:209, 2003.
[11] K. Schmid and J. Roth. *J. Nucl. Mater.*, 313–316:302, 2003.
[12] R. Neu, R. Dux, A. Kallenbach, and et. al. T. Pütterich. *Nucl. Fusion*, 45:209, 2005.

Table captions

Table. 1
Table of input parameters used in the ion trajectory ray tracing calculation for the flux and erosion distributions.

Figure captions

Fig. 1
SEM image of the erosion pattern on a W coated C tile from the outer divertor of ASDEX-Upgrade. The image was recorded in secondary electron (SE) mode.

Fig. 2
Combination of the surface topography measured by AFM and the SEM based erosion pattern. At the red marked surface areas full W erosion is observed in the SEM image.

Fig. 3
Coordinate system used in the model. Also shown are average impact directions for different impinging ions.

Fig. 4
Schematic drawing of the model applied to calculate the electric fields in the plasma boundary sheath.

Fig. 5
View along the y axis a.) and the -x axis b.) onto the final gyration of a particle prior to entering the sheath region.

Fig. 6
Impact angle distributions for long range transport D^+ and C^+4, and promptly re-deposition W^+1 using the input parameters in Table 1.

Fig. 7
Comparison of impact angle distributions using the input parameters in Table 1 with versus without the influence of an electric field.

Fig. 8
Histogram of the relative variation of the average impact angle during variation of the input parameters in Table 1 according to row "Variation range" for D, C^{+4} and W^{+1} ions.

Fig. 9

Illustration of the processes that influence the flux distribution on a rough surface.

Fig. 10

Distribution of normal vector components as obtained from the AFM topography data in Fig. 2.

Fig. 11

Distributions calculated by trajectory ray tracing for C^{+4} ions using the parameters in Table 1. Ion flux: a.) Effective W sputter yield b.) and gross erosion flux c.)

Fig. 12

Flux distribution of promptly re-deposited W^{+1} using the parameters in Table 1.

Fig. 13

Spatial distribution of the net erosion depth (μm) calculated using the parameters in Table 1 and a fraction of 0.3% C^{+4} in the incident flux.

Table 1.

Parameter	B (T)	δ (°)	T_e (eV)	n_e (m^{-3})	$\frac{v_{\|\|}}{c_s}$
Central value	1	5	20	10^{18}	1
Variation range	0.5-2	4-10	$10 - 30$	$10^{18} - 10^{19}$	0.1 - 1

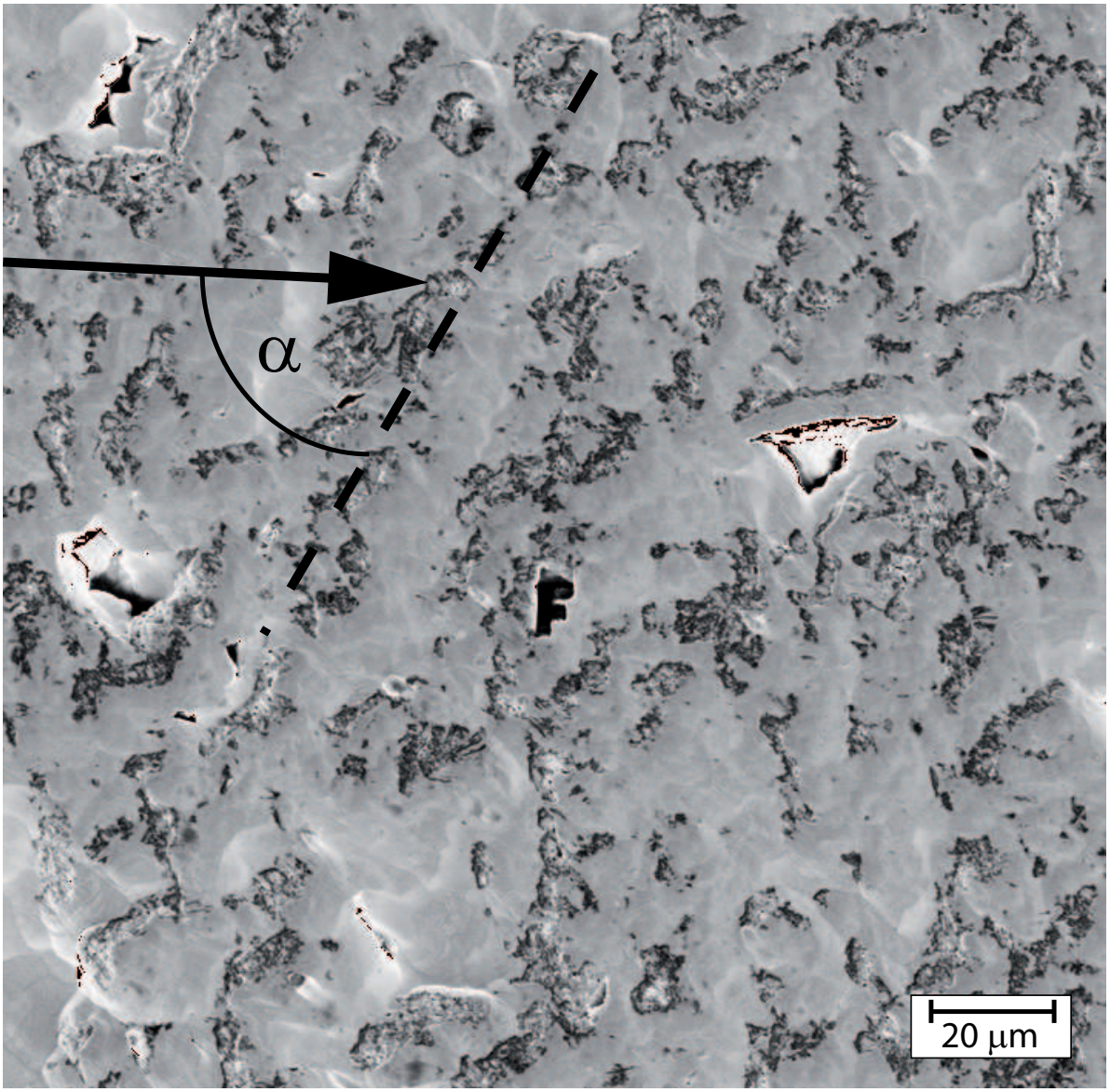

Figure 1.

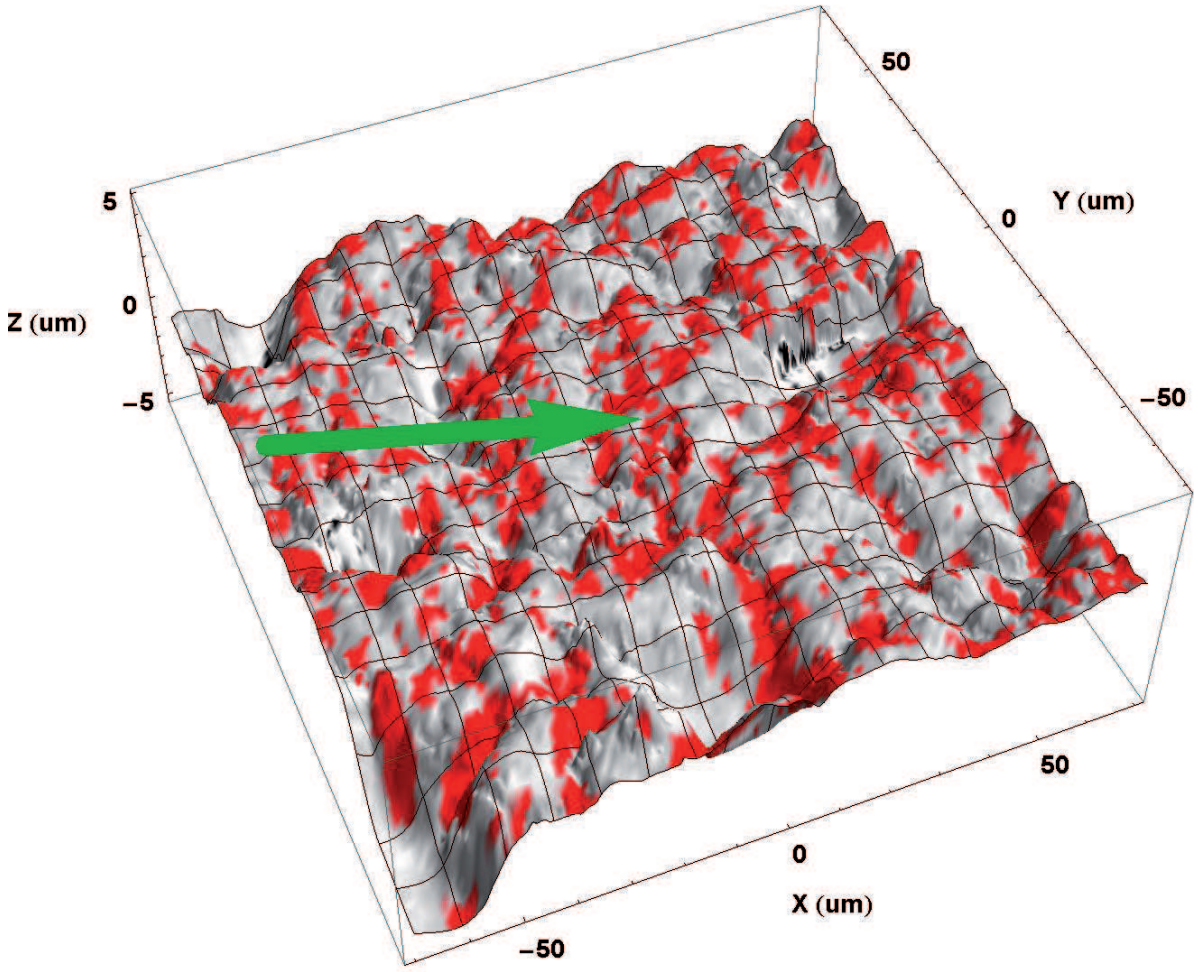

Figure 2.

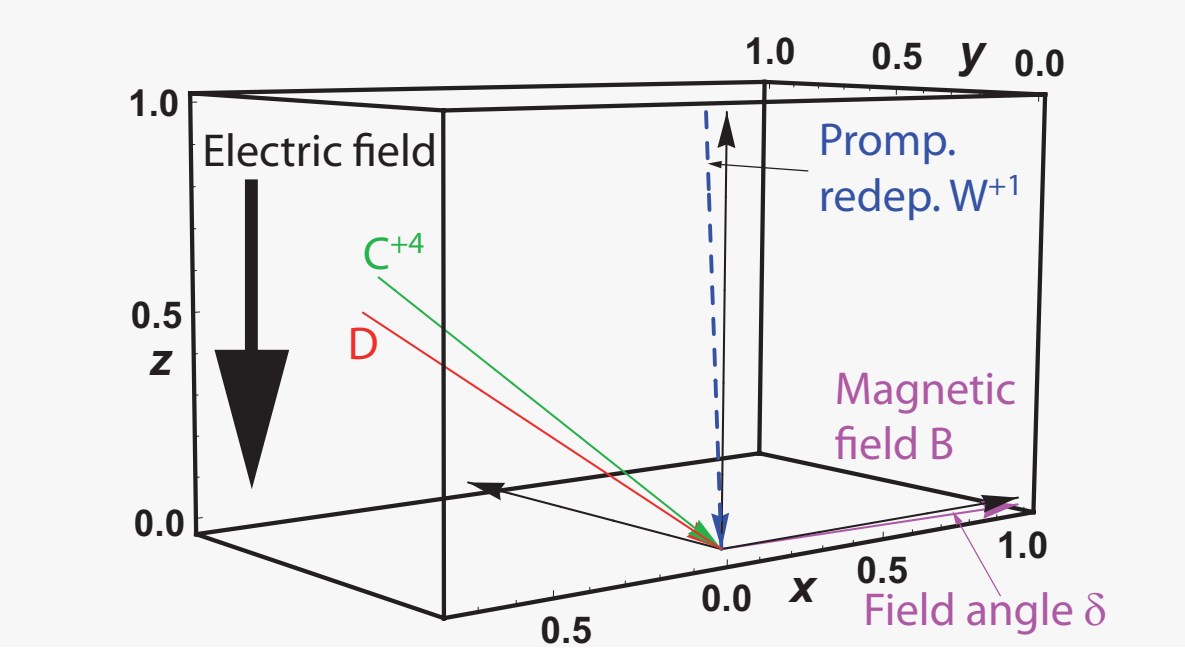

Figure 3.

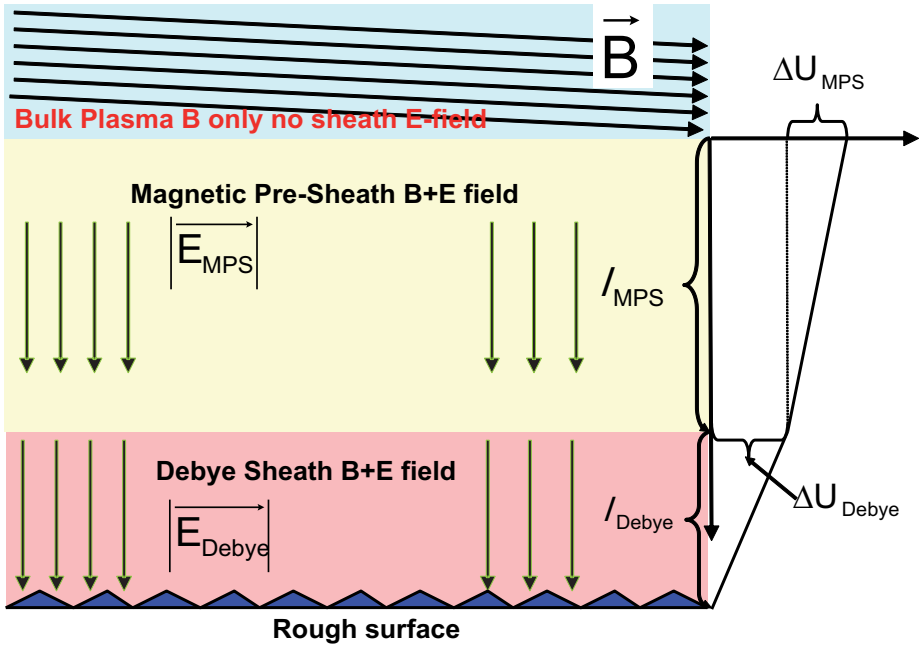

Figure 4.

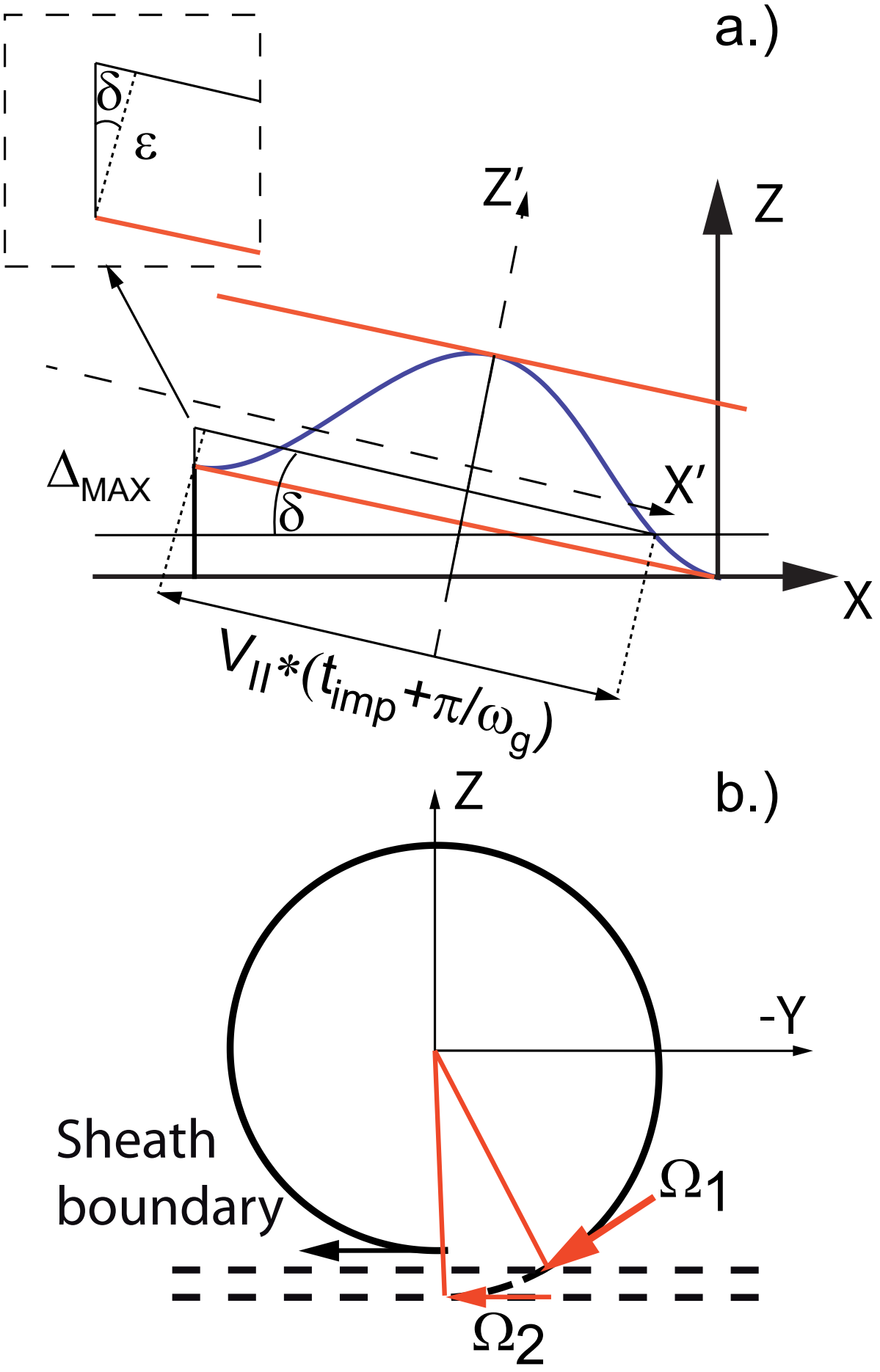

Figure 5.

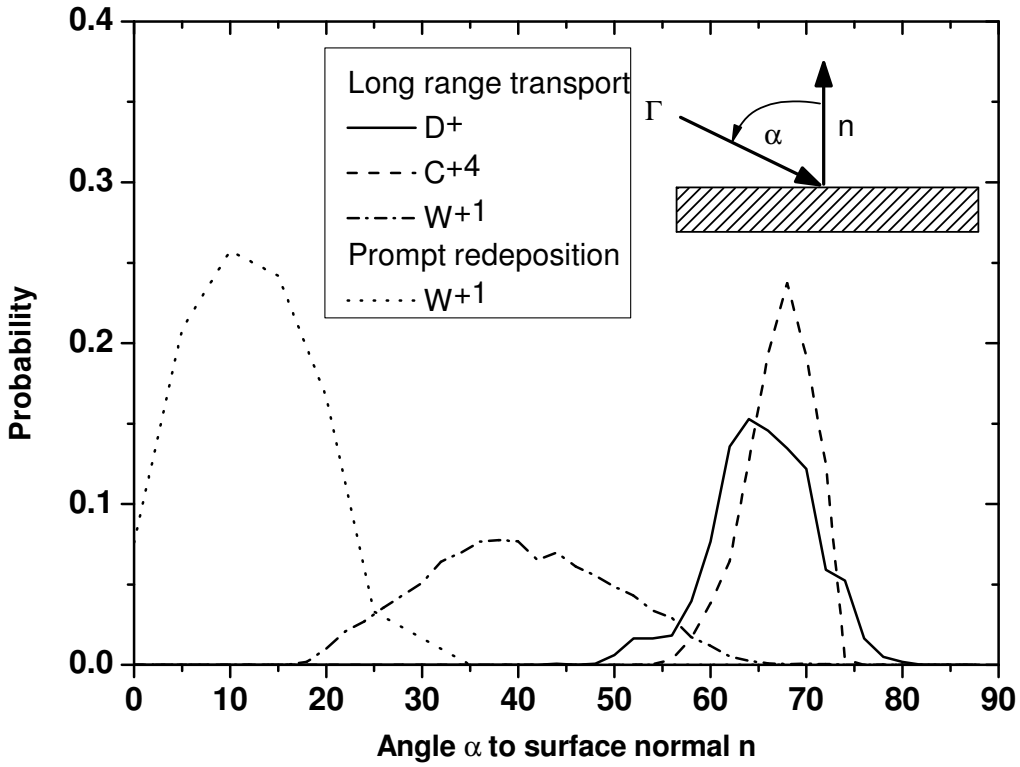
Long range transport
D+
C+4
W+1
Prompt redeposition
W+1
Γ
α
n
Probability
Angle α to surface normal n
0.0
0.1
0.2
0.3
0.4
0
10
20
30
40
50
60
70
80
90

Figure 6.

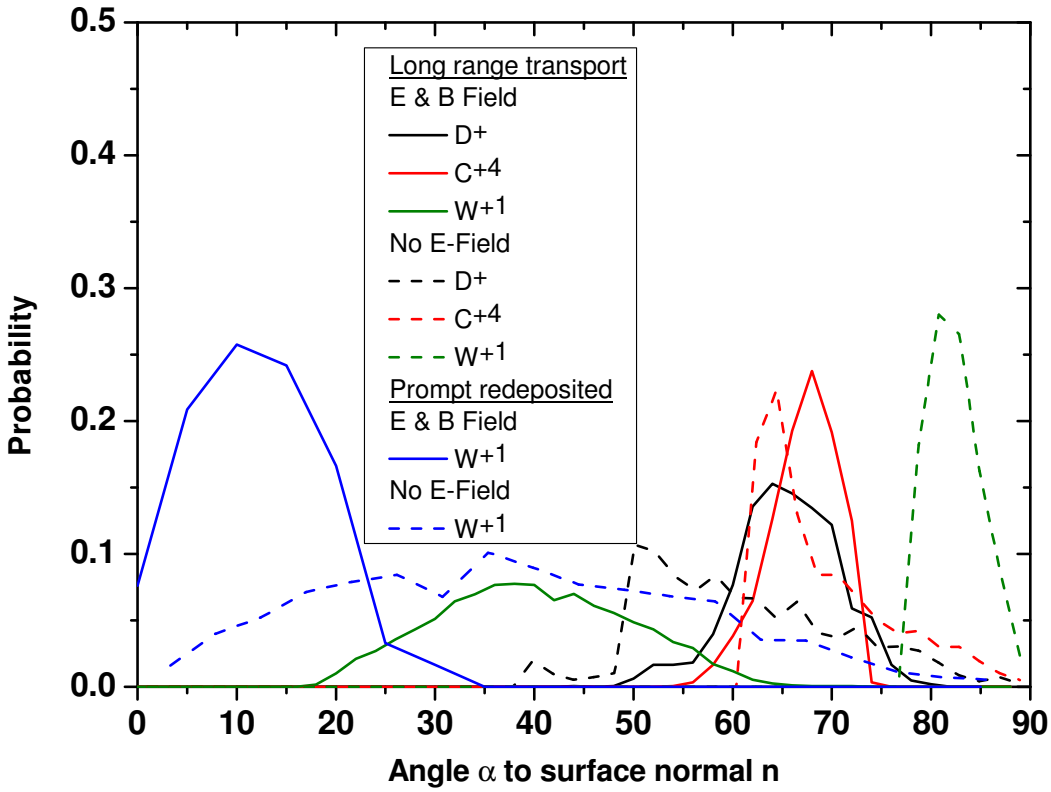
Long range transport
E & B Field
D+
C+4
W+1
No E-Field
D+
C+4
W+1
Prompt redeposited
E & B Field
W+1
No E-Field
W+1
Probability
Angle α to surface normal n
0.0
0.1
0.2
0.3
0.4
0.5
0
10
20
30
40
50
60
70
80
90

Figure 7.

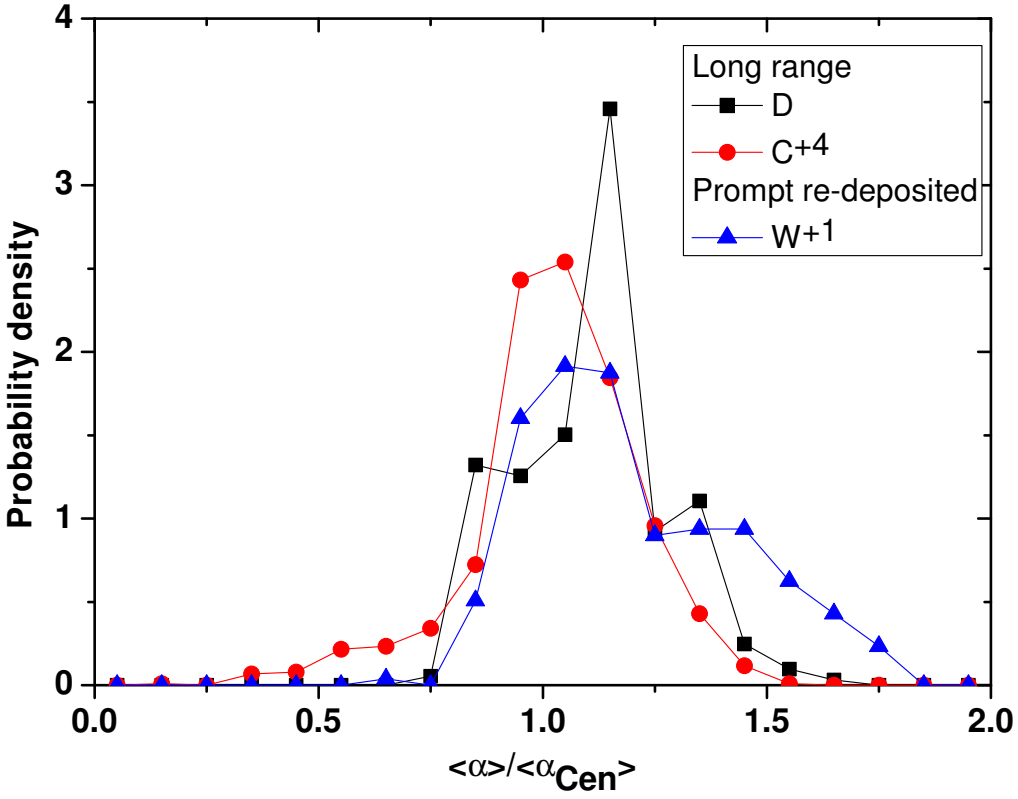

Figure 8.

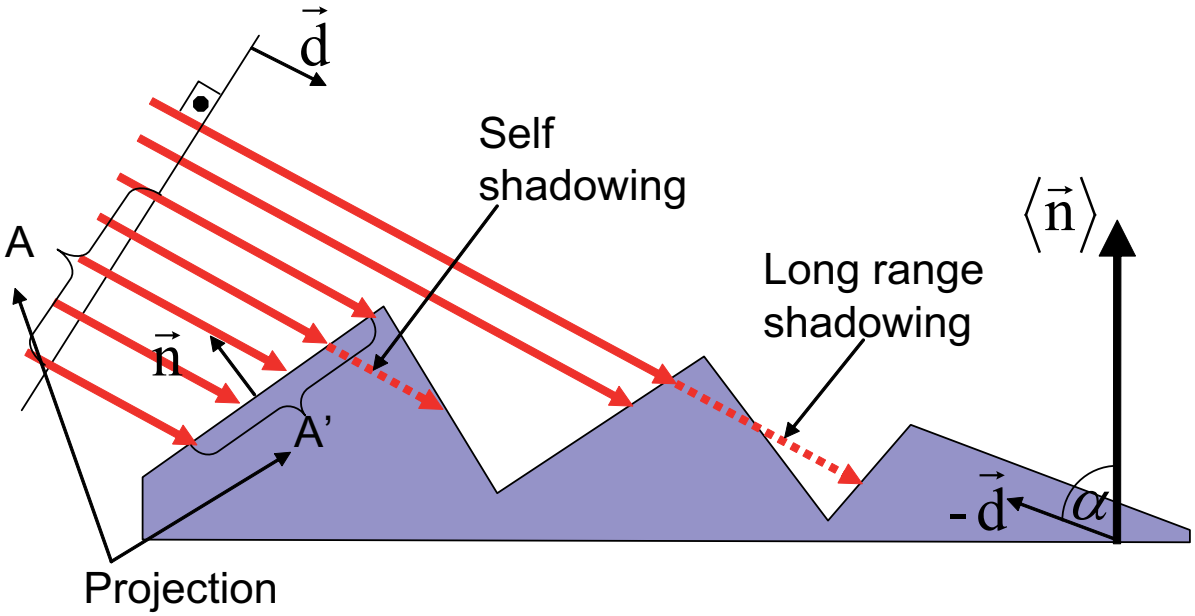

Figure 9.

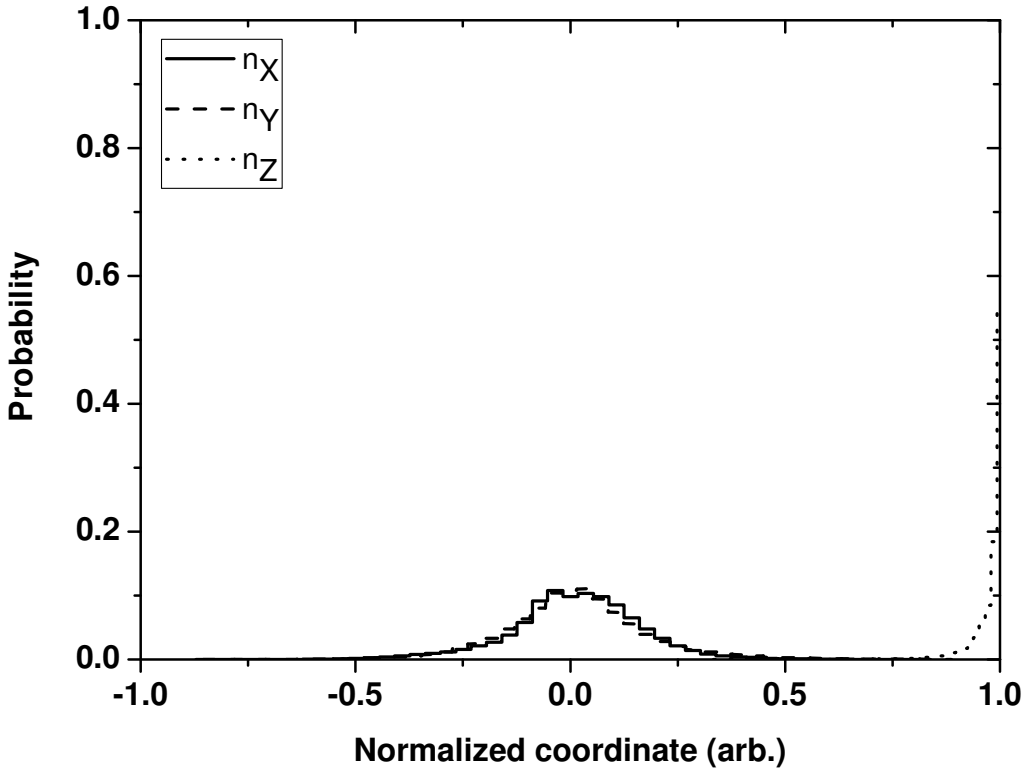
1.0
0.8
0.6
0.4
0.2
0.0
Probability
n_X
n_Y
n_Z
-1.0
-0.5
0.0
0.5
1.0
Normalized coordinate (arb.)

Figure 10.

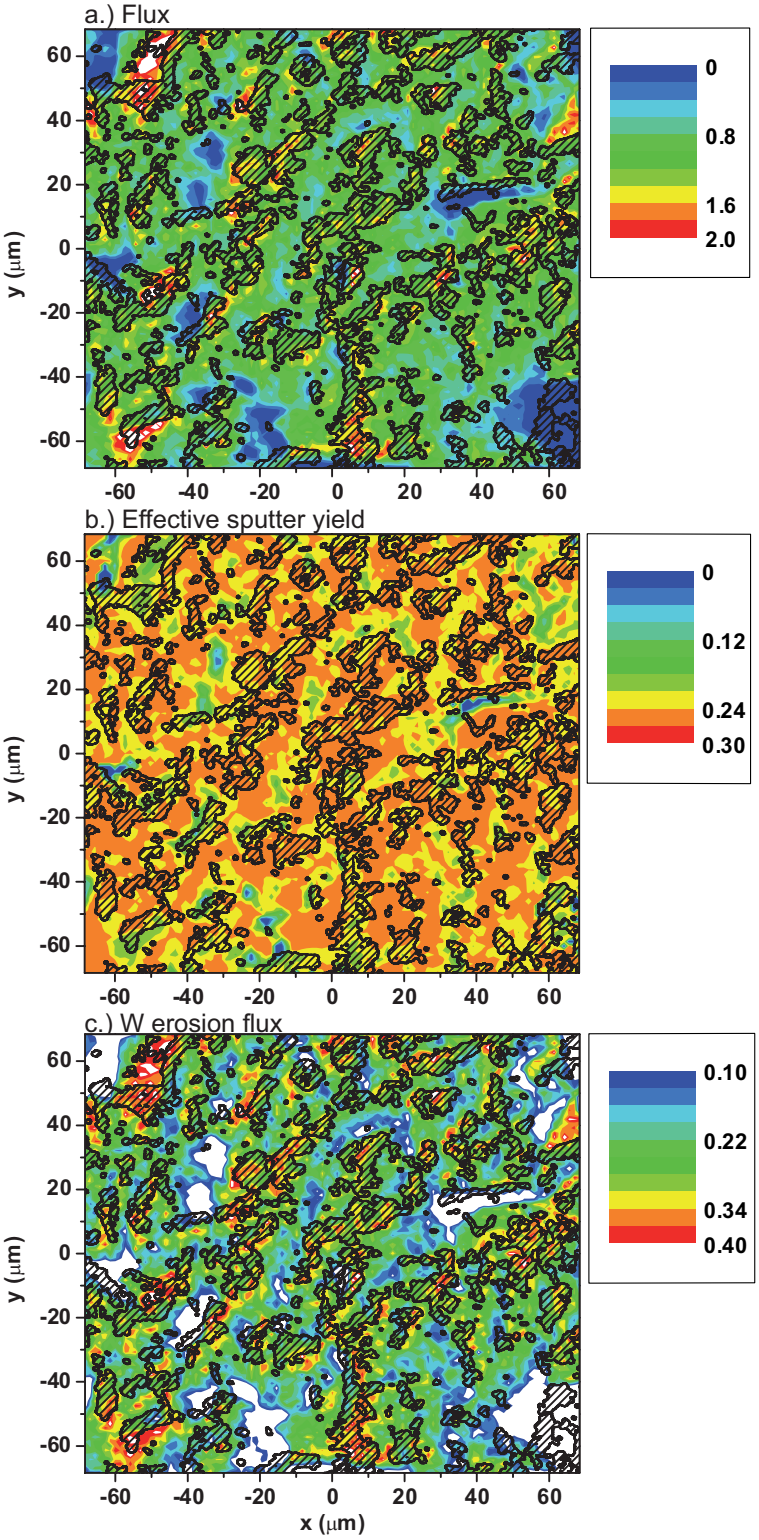
a.) Flux
0
0.8
1.6
2.0
b.) Effective sputter yield
0
0.12
0.24
0.30
c.) W erosion flux
0.10
0.22
0.34
0.40
y (μm)
x (μm)
60
40
20
0
-20
-40
-60

Figure 11.

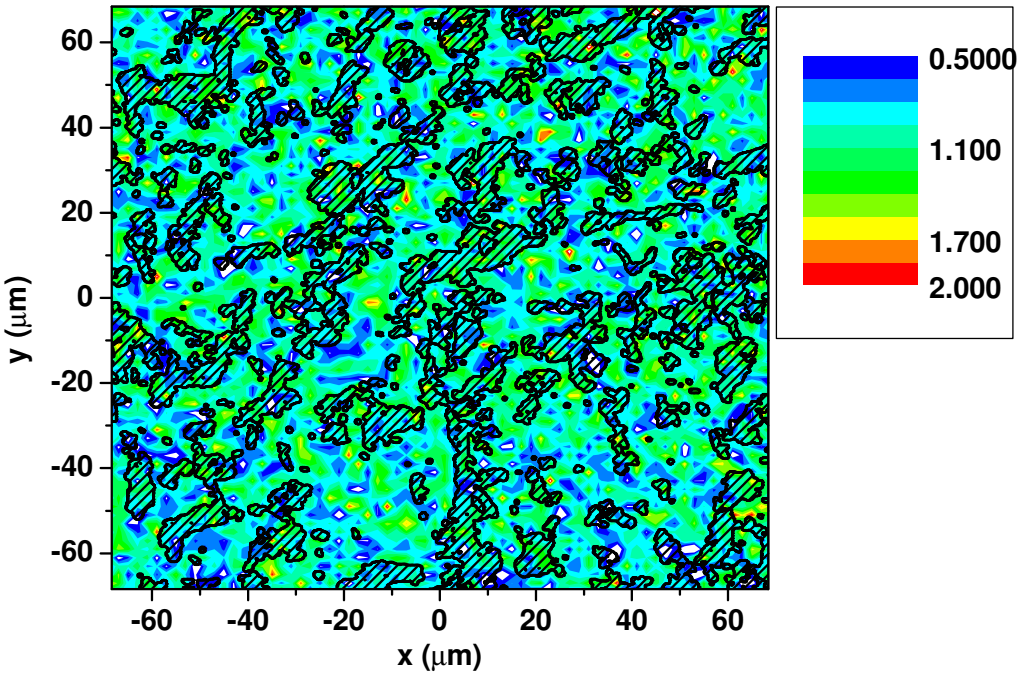

Figure 12.

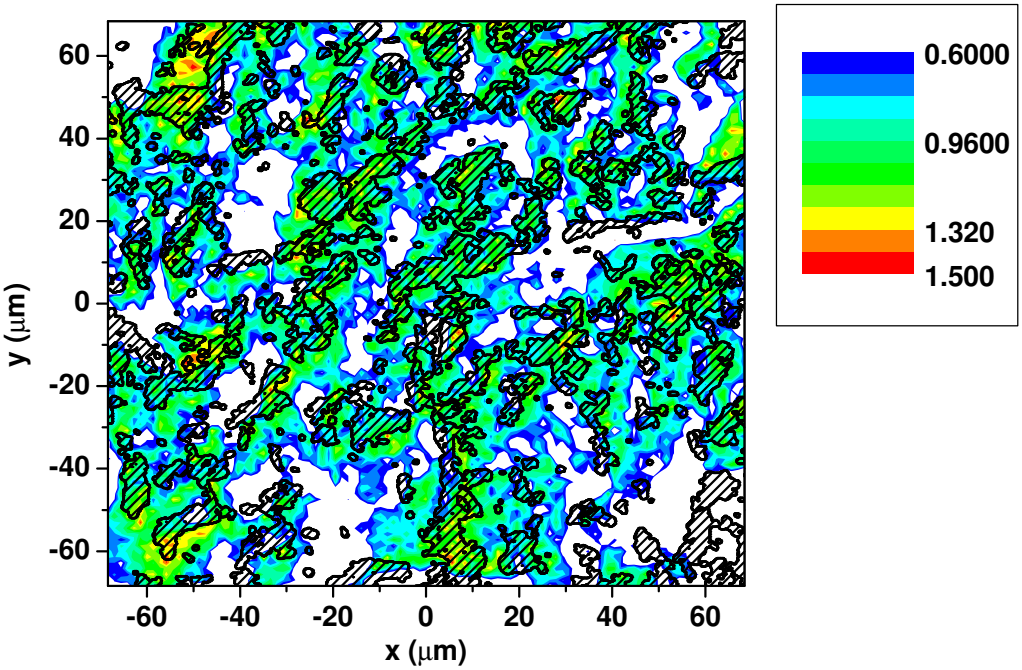
60
40
20
0
-20
-40
-60
y (μm)
-60
-40
-20
0
20
40
60
x (μm)
0.6000
0.9600
1.320
1.500

Figure 13.